ADVANCES IN ATMOSPHERIC SCIENCES, VOL. 31, MARCH 2014, 421–434

# Impacts of the Lowest Model Level Height on Tropical Cyclone Intensity and Structure

MA Zhanhong, FEI Jianfang*, HUANG Xiaogang, and CHENG Xiaoping

*College of Meteorology and Oceanography, PLA University of Science and Technology, Nanjing* 211101

(Received 1 March 2013; revised 30 June 2013; accepted 1 July 2013)

ABSTRACT

Variable thicknesses in the lowest half-$\eta$ model level (LML) are often used in atmospheric models to compute surface diagnostic fields such as surface latent and sensible heat fluxes. The effects of the LML on simulated tropical cyclone (TC) evolution were investigated in this study using the Weather Research and Forecasting (WRF) model. The results demonstrated notable influences of the LML on TC evolution when the LML was placed below 12 m. The TC intensification rate decreased progressively with a lowering of the LML, but its ultimate intensity change was relatively small. The maximum 10-m winds showed different behavior to minimum sea level pressure and azimuthally-averaged tangential winds, and thus the wind–pressure relationship was changed accordingly by varying the LML. The TC circulation was more contracted in association with a higher LML.

Surface latent heat fluxes were enhanced greatly by elevating the LML, wherein the wind speed at the LML played a dominant role. The changes in the wind speed at the LML were dependent not only on their profile differences, but also the different heights they were taken from. Due to the enhanced surface heat fluxes, more intense latent heat release occurred in the eyewall, which boosted the storm's intensification. A higher LML tended to produce a stronger storm, and therefore the surface friction was reinforced, which in turn induced stronger boundary layer inflow together with increased diabatic heating.

**Key words**: tropical cyclone, lowest model level, simulation

**Citation**: Ma, Z. H., J. F. Fei, X. G. Huang, and X. P. Cheng, 2014: Impacts of the lowest model level height on tropical cyclone intensity and structure. *Adv. Atmos. Sci.*, **31**(2), 421–434, doi: 10.1007/s00376-013-3044-9.

## 1. Introduction

The surface layer (SL), which is defined as the lowest layer of the atmosphere, is conventionally referred to as the region at the bottom 10% of the planetary boundary layer (PBL; Stull, 1988; Holton, 2004). Its depth ranges from a few meters to more than 100 m, depending on the stability of its thermal stratification. Within the SL, meteorological variables such as wind speed, temperature and humidity change rapidly with height and the most significant air–sea energy exchange occurs (Arya, 1988). Thus, it is crucial to represent accurate SL characteristics in numerical models. Most of the current SL parameterization schemes compute surface sensible and latent heat fluxes and friction velocities using variables at the lowest half-$\eta$ model level (LML) on behalf of the SL state, assuming that the LML is within or at the top of the real SL.

The impacts of the LML height have been investigated in a few studies (Wei et al., 2001; Zängl et al., 2008; Aligo et al., 2009; Shin et al., 2012). Wei et al. (2001) explored the influence of the LML height on a snowmelt event and suggested that an LML with a height of less than 10 m is expected to accurately simulate the snowmelt. On the other hand, if the LML is placed above the real SL, the surface heat fluxes could be underestimated by as much as 40%. Based on simulations of an alpine foehn, Zängl et al. (2008) showed that the LML height has greater influence even than the selection of PBL scheme and that simulations are improved when moving the LML closer to the surface. Aligo et al. (2009) also demonstrated that lowering the height of the LML is necessary for improving quantitative precipitation forecasts. These aforementioned studies all focused on stable SL conditions and suggested adopting a low LML height, e.g., below 10 m. Recently, Shin et al. (2012) carried out a series of experiments under both stable and unstable SL conditions to examine impacts of the LML on PBL structures. They found that surface variables are almost insensitive to the LML height when it is above 12 m in daytime, but are systematically altered as the LML height is lowered below 40 m at nighttime.

Unlike the aforementioned weather events, a tropical cyclone (TC) obtains its energy via transport of surface heat fluxes from the underlying ocean surface (Emanuel, 1986)

* Corresponding author: FEI Jianfang
Email: feijf@sina.com.cn

and exhibits little diurnal variation, which could make the roles of the LML different. The storm boundary layer is typically 0.5–1 km deep, rising with the increasing radius near the inner core of a TC (Kepert and Wang, 2001; Smith et al., 2010). Hence, it seems that an appropriate placement of the LML should not be higher than 50 m given the conventional definition of the SL. Although the influences of vertical model resolution on tropical cyclone modeling have been examined in previous works (e.g., Zhang and Wang, 2003; Kimball and Dougherty, 2006), systematic investigations of the impact of the LML have been few, despite its unique role in numerical models. Zhang and Wang (2003) suggested that adopting a thicker surface layer would produce stronger surface winds. By diagnosing the impacts of different distributions of vertical levels, Kimball and Dougherty (2006) stated that surface heat fluxes could be overvalued if the LML is placed "too high". Nonetheless, in their sensitivity experiments, not only was the LML distributed differently, but also the other vertical levels, which may have confused the real influences of the LML.

The aim of this study is to investigate how a simulated TC is influenced by the selection of LML, especially when the LML is placed within the SL of the real atmosphere. Section 2 describes the model configuration and experimental design. A brief introduction to the SL and PBL parameterization is provided in section 3. Section 4 discusses the model results in detail, with a focus on the effect of the LML height on TC intensification and structural changes. A discussion is presented in section 5, and a summary of the main conclusions of the study is given in section 6.

## 2. Model configuration and experimental design

The Weather Research and Forecasting (WRF) model (version 3.2; Skamarock et al., 2008) was used in this study. This model utilizes a terrain-following hydrostatic-pressure vertical $\eta$ coordinate, which is defined as

$$\eta = (p - p_t)/(p_s - p_t) \,, \tag{1}$$

where $p$ is pressure, $p_s$ is the pressure along the model surface boundary, and $p_t$ is the pressure along the model top boundary, which was set to 50 hPa.

All experiments were performed on an $f$-plane centered at 20°N, using two-way interactive nested meshes with dimensions of $220 \times 220$ and $202 \times 202$, and resolutions of 15 km and 5 km, respectively. The authors admit that although a resolution of 5 km is capable of reproducing a TC's intensity evolution and primary structural features (Ma et al., 2013), a much finer resolution would have been superior in terms of resolving more detailed TC structures (Yau et al., 2004; Gentry and Lackmann, 2010; Chen et al., 2011). The outer domain utilized the Kain–Fritsch scheme (Kain, 2004) to parameterize the cumulus processes, while no cumulus parameterization was used in the inner mesh. The Lin scheme (Lin et al., 1983) was used to model the microphysical processes. The Dudhia shortwave (Dudhia, 1989) and Rapid Radiative Transfer Model (RRTM) longwave (Mlawer et al., 1997) schemes were used as the radiation schemes, while the Yonsei University (YSU) scheme (Hong et al., 2006) with some modification (which will be discussed in section 3) was chosen as the PBL scheme.

The quiescent and horizontally-uniform environmental fields were specified according to the mean tropical sounding of temperature and humidity profiles given by Jordan (1958). The underlying model boundary was set uniformly to be the sea surface with a constant temperature of 28°C and a surface pressure of 1010 hPa. An axisymmetric cyclonic vortex similar to that used by Stern and Nolan (2011) was then implanted in this idealized atmosphere environment, with a maximum wind speed of 24 m s$^{-1}$ at the radius of 125 km and height of 1.5 km. The vortex was in hydrostatic and gradient wind balance and basically remained stationary during the simulation. The model was integrated for a total of 132 h.

The model possessed 29 full-$\eta$ vertical levels, of which 28 are distributed as default in WRF, but one additional level was added as the second lowest full-$\eta$ level ($\eta_2$), with its height varying for different runs, thus meaning the height of the LML changed accordingly. A total of five experiments with the LML placed at 20m, 12m, 8m, 6m and 4m were conducted and denoted as H20, H12, H08, H06 and H04, respectively. Table 1 shows the detail of these experiments, including information of the LML and the lowest four full-$\eta$ levels.

## 3. The SL and PBL parameterization

Monin–Obukhov similarity theory (Monin and Obukhov, 1954) is a widely used framework of current SL schemes. In the current WRF version, each SL scheme must be tied to a specified PBL scheme. The SL scheme uses stability functions (Paulson, 1970; Dyer and Hicks, 1970; Webb, 1970; Jiménez et al., 2012) to compute dimensionless surface exchange coefficients for heat ($C_h$), moisture ($C_q$), and momen-

**Table 1.** List of numerical experiments.

| Expt | Height of LML (m) | $\eta_a$ | $\eta_1$ | $\eta_2$ | $\eta_3$ | $\eta_4$ |
|---|---|---|---|---|---|---|
| H20 | 20 | 0.9975 | 1.0 | 0.995 | 0.99 | 0.978 |
| H12 | 12 | 0.9985 | 1.0 | 0.997 | 0.99 | 0.978 |
| H08 | 08 | 0.999 | 1.0 | 0.998 | 0.99 | 0.978 |
| H06 | 06 | 0.99925 | 1.0 | 0.9985 | 0.99 | 0.978 |
| H04 | 04 | 0.9995 | 1.0 | 0.999 | 0.99 | 0.978 |

tum ($C_{d10}$):

$$C_h = \frac{k^2}{\left[\ln\left(\frac{z_a}{z_0}\right) - \psi_m\left(\frac{z_a}{L}\right)\right]\left[\ln\left(\frac{z_a}{z_0}\right) - \psi_h\left(\frac{z_a}{L}\right)\right]} , \quad (2)$$

$$C_q = \frac{k^2}{\left[\ln\left(\frac{z_a}{z_0}\right) - \psi_m\left(\frac{z_a}{L}\right)\right]\left[\ln\left(\frac{\rho c_p u_* z_a}{c_s} + \frac{z_a}{z_0}\right) - \psi_h\left(\frac{z_a}{L}\right)\right]} , \quad (3)$$

$$C_{d10} = \frac{k^2}{\left[\ln\left(\frac{10}{z_0}\right) - \psi_m\left(\frac{10}{L}\right)\right]^2} , \quad (4)$$

where $k$ is the von Karman constant, $z_0$ is the roughness length, $z_a$ is the height of the LML, $L$ is the Monin–Obukhov length, $\rho$ is the air density in the SL, $c_p$ is specific heat at constant pressure, $u_*$ is the friction velocity and $c_s$ is the effective heat transfer coefficient, which is related to the molecular transport (Zhang and Anthes, 1982); $\psi_m$ and $\psi_h$ are the similarity stability functions for momentum and heat. Note that $z_a$ is used to compute $C_h$ and$C_q$, while 10 m is used to compute $C_{d10}$. Over the water surface the SL scheme calculates surface fluxes directly, which are used by the PBL scheme to provide tendencies of temperature, moisture, and momentum in the boundary layer. In a bulk formula framework, the surface fluxes are parameterized as follows:

$$\mathrm{HFX} = \rho c_p C_h U_a(\theta_g - \theta_a) , \quad (5)$$

$$\mathrm{QFX} = \rho L_v C_q U_a(q_g - q_a) , \quad (6)$$

$$\tau = \rho u_*^2 = \rho C_{d10} U_{10}^2 , \quad (7)$$

where HFX, QFX and $\tau$ are the fluxes of sensible heat, latent heat and momentum; $U$ is the horizontal wind speed, $L_v$ is the latent heat of vaporization, $\theta$ is the potential temperature, and $q$ is the mixing ratio of water vapor. The subscripts "a", "10" and "g" denote the LML, 10 m and bottom surface, respectively; $q_g$ denotes the ground saturation specific humidity (Zhang and Anthes, 1982), which is outputted directly from the WRF model. $U_{10}$ is diagnosed through $U_a$ using similarity theory:

$$U_{10} = \frac{\ln\left(\frac{10}{z_0}\right) - \psi_m\left(\frac{10}{L}\right)}{\ln\left(\frac{z_a}{z_0}\right) - \psi_m\left(\frac{z_a}{L}\right)} U_a . \quad (8)$$

Note that $U_{10}$ is derived from $U_a$ by interpolation for $z_a$ higher than 10 m, but by extrapolation for $z_a$ lower than 10 m.

The YSU scheme used in this study has performed satisfactorily in some previous TC simulations (e.g., Nolan et al., 2009a, 2009b). It is a nonlocal closure PBL scheme using a K-profile approach to represent the mixing within the boundary layer under convective conditions. Therefore, the depth of the PBL should be first estimated. In the YSU scheme, the PBL height is defined as (Hong et al., 2006):

$$\frac{gH}{|U(H)|^2}\left[\frac{\theta_v(H) - \theta_{va} - \theta_T}{\theta_{va}}\right] = Ri_c , \quad (9)$$

where $H$ is the PBL height, $\theta_v$ is the virtual potential temperature, $\theta_{va}$ is the virtual potential temperature at the LML, and $\theta_T$ is the virtual temperature excess of thermals. $Ri_c$ is the critical bulk Richardson number, which equals zero under convective boundary layer conditions. The stability of the PBL in the YSU scheme is determined by the bulk Richardson number ($Ri_B$) in the SL:

$$Ri_B = \frac{g z_a(\theta_{va} - \theta_{vg})}{\theta_a |U_a|^2} . \quad (10)$$

The PBL is judged to be stable for $Ri_B > 0$, while convective for $Ri_B \leqq 0$. Since the $Ri_B$ is mostly, if not all, negative for all runs (not shown), Eq. (9) can be degraded as:

$$\theta_v(H) = \theta_{va} + \theta_T . \quad (11)$$

This form also serves as the basis for some common thermodynamic definitions of the TC boundary layer, with $\theta_T$ taken as 0.5 K (e.g., Anthes and Chang, 1978, Powell, 1990). To eliminate possible changes in the PBL scheme's performance caused directly by varying the LML height, a modified YSU scheme, which is relatively insensitive to the LML, was used [as proposed by Shin et al. (2012)]. That is, $\theta_T$ is excluded when the LML is within the real SL, since $\theta_{va}$ increases toward the temperature of the thermals as the LML approaches the surface (Shin et al., 2012). Actually, the commonly used LMLs were all well within the real SL in this TC case because of its convective PBL feature.

## 4. Results

### 4.1. *TC intensity, size and structure*

The evolution of TC intensity in terms of the minimum sea level pressure (MSLP) and the maximum 10-m wind (VMAX10) is shown in Fig. 1. The simulated storm in each experiment intensified in the first several days and reached maturity thereafter. Nevertheless, large discrepancies existed in their intensification processes. From Fig. 1a, H04 produced the slowest intensification rate of about 0.64 hPa $h^{-1}$ during the first 84 h, followed by H06 and H08, giving values of 0.85 hPa $h^{-1}$ and 0.9 hPa $h^{-1}$, respectively, which can be ranked according to their LML heights. H20 and H12 both possessed the most rapid intensification rate of 0.95 hPa $h^{-1}$. At 72 h, the MSLP in H20 deepened to 920 hPa, while at the same time H04 gave a value of 950 hPa, showing a difference of 30 hPa. It seems that when the LML was placed below 12 m, the storm intensification rate tended to decrease with a lowering of the LML. However, as the storms in different runs reached maturity, their ultimate intensity differences were relatively small. The evolutionary trend of VMAX10 showed similar behavior to that of MSLP before approximately 96 h (Fig. 1b), during which time the largest wind difference between H20 and H04 reached 18 m $s^{-1}$. Nonetheless, in the later stage H04 still showed obviously smaller VMAX10 than H20 and H12 for a long time, even when its MSLP was deeper than H20 and H12, an indication of the delayed evolutionary trend of MSLP in H04. The MSLP and VMAX10 have a complicated internal relationship influenced by many factors, such as storm size, intensity and

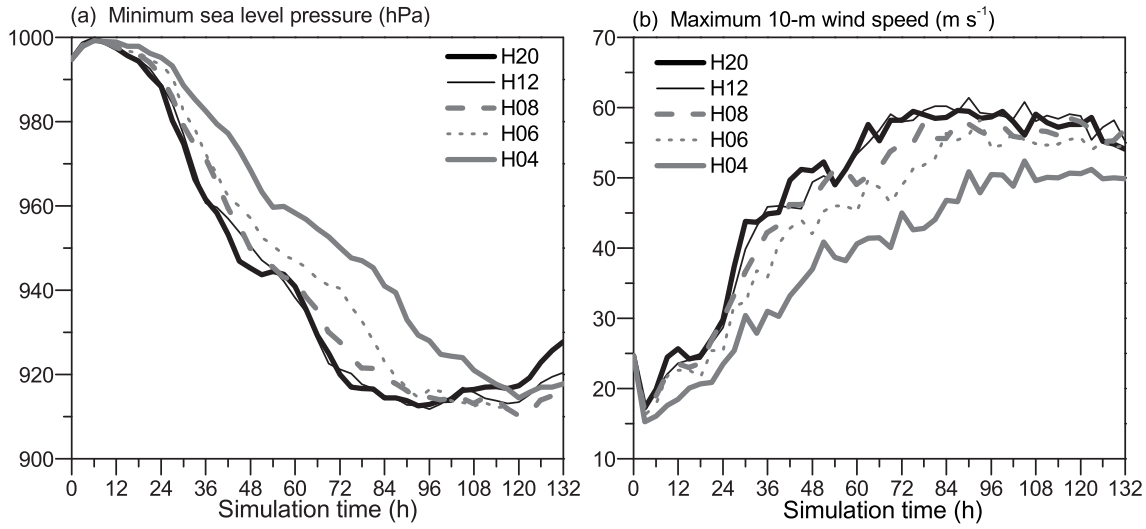


**Fig. 1.** Time evolution of (a) the minimum sea level pressure (hPa) and (b) the maximum 10-m wind speed (m $s^{-1}$).

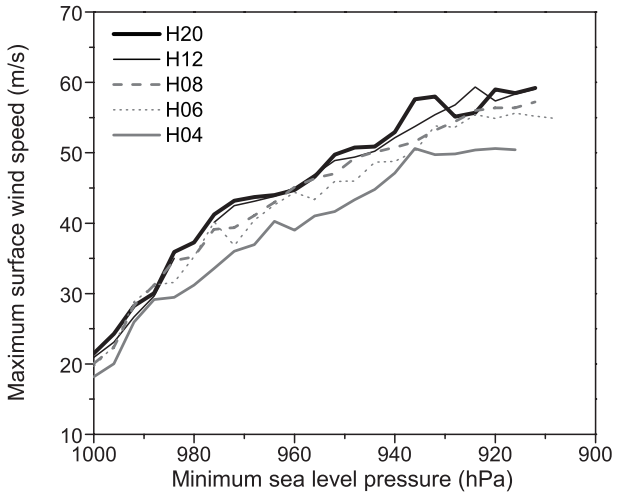


**Fig. 2.** The relationship between the maximum surface wind speed (m $s^{-1}$) and the minimum sea level pressure (hPa).

surface friction (Knaff and Zehr, 2007; Kieu et al., 2010; Bao et al., 2012). A comparison of the wind–pressure relationships from all runs (Fig. 2) indicates that the simulated wind–pressure relationship was also modulated by the selection of LML. H20 and H12 again exhibited a similar relationship, which was different from H08, H06 and H04. The more intense the storm was, the more evident their difference seemed to be. For the same MSLP, the wind difference between two runs was able to reach 8 m $s^{-1}$. Such an uncertainty in the wind–pressure relationship caused by varying the LML suggests that caution is required when examining the performance of a numerical model in reproducing the wind–pressure relationship, especially when the LML is placed below 12 m. To facilitate exploring the roles of varying the LML in determining the storm intensity, the following analysis focuses mainly on the results of H20 and H04 due to their large discrepancies and consistencies with other experiments.

From the Hovmöller diagrams of the low-level tangential winds (Fig. 3), we can see that the storm in H04 intensified more slowly and gave weaker intensity than in H20 in the early stage. However, it still strengthened after the storm in H20 reached maturity, and eventually possessed larger maximum winds after about 114 h. A diagnosis of tangential winds at other levels also revealed similar results (not shown). This intensity relationship resembled that expressed by MSLP, but was conflicting to that by VMAX10. Such an inconsistency between VMAX10 and other intensity terms such as MSLP and low-level tangential winds was also found by Bao et al. (2012), who thus recommended tangential winds as an additional measure of storm intensity together with MSLP and VMAX10. As discussed above, the 10-m winds were not computed directly by the model, but diagnosed from $U_a$ using a semi-empirical relationship [Eq. (8)]. For varying the LML, the $U_{10}$ was derived by interpolation or extrapolation from different heights; therefore, its value may have had some bias compared to the true value due to the changes of slope rate in Eq. (8), which could partly explain why the behavior of VMAX10 was inconsistent to that of MSLP or the low-level tangential winds. Therefore, for numerical experiments with the same LML, taking the maximum winds at the LML on behalf of the storm intensity seems to be superior to taking the 10-m winds, if not verifying the model outputs against 10-m observational data. Accompanying the TC intensification, the radius of maximum tangential winds (RMW) in each experiment contracted rapidly initially due to the spin-up process and then evolved slowly. Compared with H20, H04 produced larger RMW after the spin-up period that contracted continuously after the initial rapid contraction, and therefore their difference in RMW was reduced gradually. The storm size (indicated by the 25-m $s^{-1}$ contour) was found to be somewhat correlated to the storm intensity, demonstrating that the storm circulation enlarged with intensification of the storm. Nonetheless, the storm in

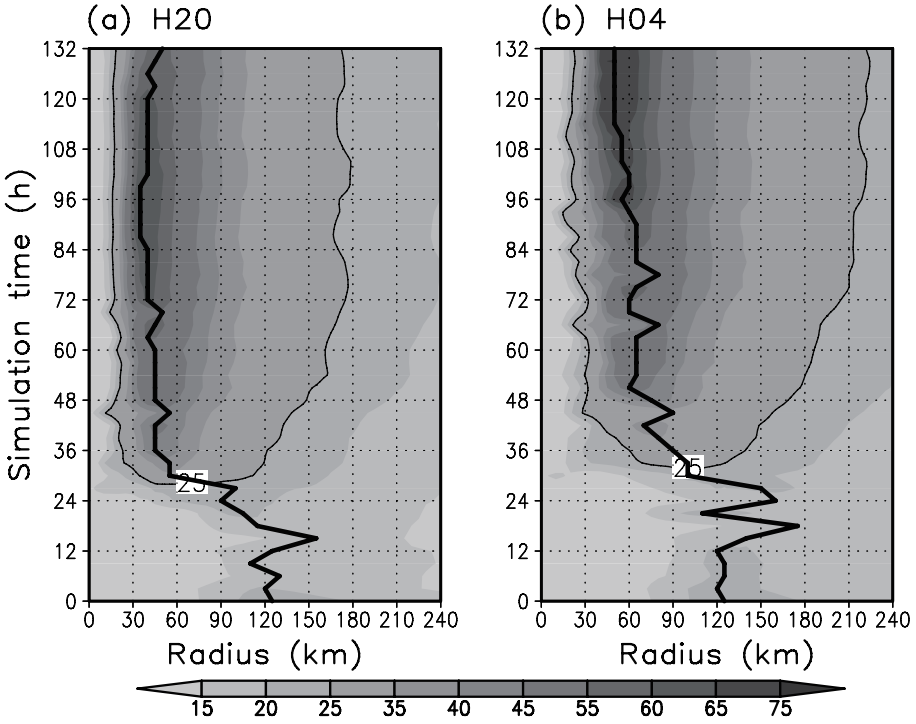


**Fig. 3.** Hovmöller diagram of the azimuthally-averaged tangential winds (m $s^{-1}$) for (a) H20 and (b) H04 at 0.1 km in altitude. The contour line indicates the radius of 25-m $s^{-1}$ tangential wind. The radius of maximum tangential winds is also shown by the thick solid line.

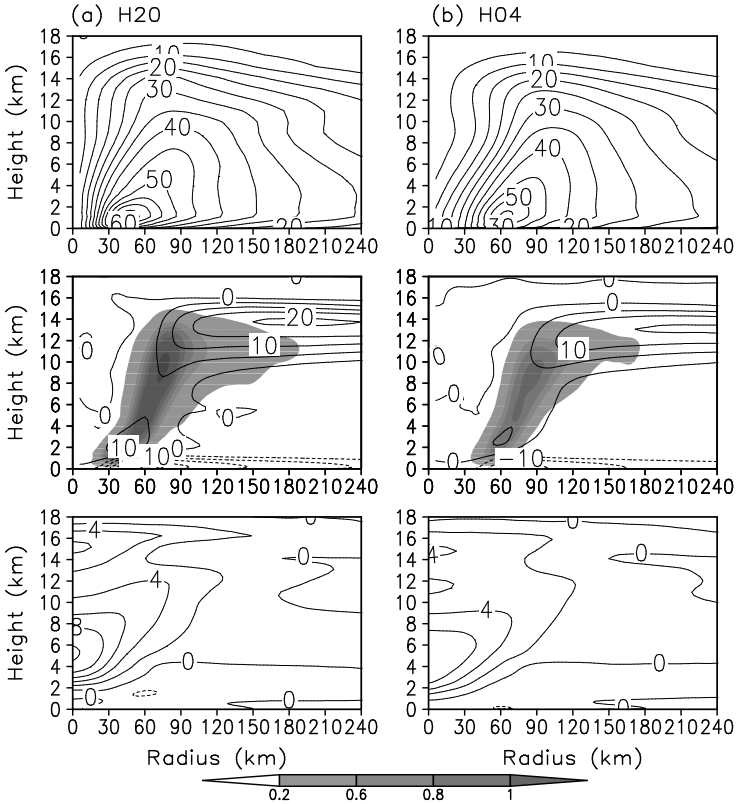


**Fig. 4.** Height–radius cross sections of the temporally- and azimuthally-averaged (a, d) tangential winds (m $s^{-1}$), (b, e) radial winds (contour, m $s^{-1}$) and vertical motion (shaded, m $s^{-1}$), and (c, f) temperature anomaly (K) from 48–60 h for (left) H20 and (right) H04.

H04 became progressively larger in size compared to that in H20, even when its intensity was weaker in the early period. At 96 h, the radius of 25-m $s^{-1}$ wind in H04 was about 50 km larger than in H20. Although the surface heat fluxes in H20 were evidently larger than in H04 (will be shown later), the storm in H20 possessed unexpectedly smaller size. This is because the larger (smaller) tangential wind gradient in H20 (H04) had produced more rapid (slower) filamentation (Wang, 2008a, 2008b). As a result, the inner rainband activity may have been greatly suppressed in H20, whereas the inner rainbands were relatively more active in H04. Therefore, the storm with active spiral rainbands showed a clearly larger inner-core size through outward expansion of tangential winds (Xu and Wang, 2010a).

The symmetric structures in terms of tangential winds, secondary circulation and temperature anomalies in H20 and H04 were similar to real TC structures after a spinup period of 48 h (Fig. 4). The maximum tangential winds occurred approximately at a radius of 40 km for H20 and 65 km for H04 (Figs. 4a, d). Figures 4b and e exhibit typical secondary circulation: the radial inflow in the boundary layer, radial outflow in the upper troposphere, and slantwise upward motion. Both H20 and H04 clearly had a warm-core structure centered at about 5 km and a secondary maximum in the upper troposphere (Figs. 4c, f; Stern and Nolan, 2012), with the latter being the key to the rapid intensification of a TC (Zhang and Chen, 2012). The tangential winds, secondary circulation, and warm-core structure were more strengthened in H20 than in H04, consistent with the intensity relationships. Equation (11) indicates that the boundary-layer depth is directly related to the virtual potential temperature at the LML. From Fig. 5, the boundary-layer depths for both runs were less than 1 km and rose with the increasing radius in the inner core (Kepert and Wang, 2001). For the case with a lower LML, the boundary layer tended to be deeper since the value of $\theta_{va}$ was larger near the surface (Shin et al., 2012). The difference of the boundary-layer depth between H20 and H04 ranged from 100 m to 300 m, which was most significant in the inner-core region. As the storms intensified, their respective boundary-layer depths in the inner core decreased slightly, while in the outer region they increased slightly. As a consequence, the radial gradient of boundary-layer depth increased, which was presumably due to the increased radial $\theta_{va}$ gradient accompanying the strengthening of the storm.

### 4.2. *Near-surface variables*

The SL process is primarily characterized by the variables at the LML. For this reason, the near-surface variables are output directly from the model in this section to evaluate their dependence on the LML height. A storm's intensification is thermodynamically maintained by the upward interfacial heat fluxes from the underlying sea surface (Emanuel, 1986). Given that the surface latent heat fluxes were several times larger than surface sensible heat fluxes (not shown), and thus accounted for the majority of the energy supplied from the ocean, the evolution of surface latent heat fluxes was analyzed on behalf of the total surface enthalpy fluxes, as shown in Fig. 6a. By lowering the LML, the surface latent heat fluxes were reduced greatly such that at 87 h the latent heat fluxes in H20 were 200 W $m^{-2}$ (34%) larger than in H04. Of interest is that, despite the unanimously larger surface heat fluxes in H20, the storm did not intensify correspondingly. Instead, after about 114 h H20 showed a weaker storm than H04 in terms of MSLP (Figs. 1a and 3), indicating that besides the surface heat fluxes, other factors modulating the storm's development were changed due to the LML variation. One possible mechanism, which requires further investigation, could be the surface friction effect, since the energy production rate is a linear function while the frictional dissipation rate is a cubic power of surface wind speed (Wang and Xu, 2010).

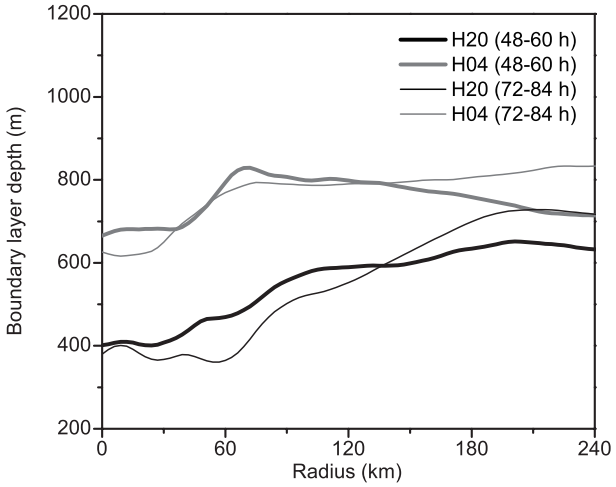


**Fig. 5.** Radial distribution of the temporally- and azimuthally-averaged PBL height (m).

According to Eq. (6), the surface latent heat fluxes are determined by the air density and wind speed at the LML, the surface exchange coefficient for moisture, and the mixing ratio difference between the surface and the LML. All these terms are displayed in Fig. 6 to investigate which factors dominated in the LML-induced changes of surface latent heat fluxes. The air density appears to have been comparatively insensitive to the LML height and exhibited no unified discrepancy between the two runs (Fig. 6b), an indication of its minor contribution to the changes in surface heat fluxes. The wind speed was much stronger in H20 (Fig. 6c), presumably due to its higher LML in addition to the differences in storm intensity (Fig. 1). The strong wind speeds helped arouse upward heat fluxes and consequently the storm strengthened, which in turn triggered more upward transport of heat fluxes based on the wind-induced surface heat-exchange (WISHE) mechanism (Emanuel, 1986). Therefore, the surface heat fluxes increased with the storm's intensification (Fig. 6a). In contrast, the surface moisture coefficient in H20 was evidently smaller than in H04, the reason for which can be speculated [from Eq. (3)] as $C_q$ tended to decrease as $z_a$ ascended. The mixing ratio difference between the surface and the LML decreased with time (Fig. 6e), probably because of the more moistened air flow induced by the enhanced surface winds

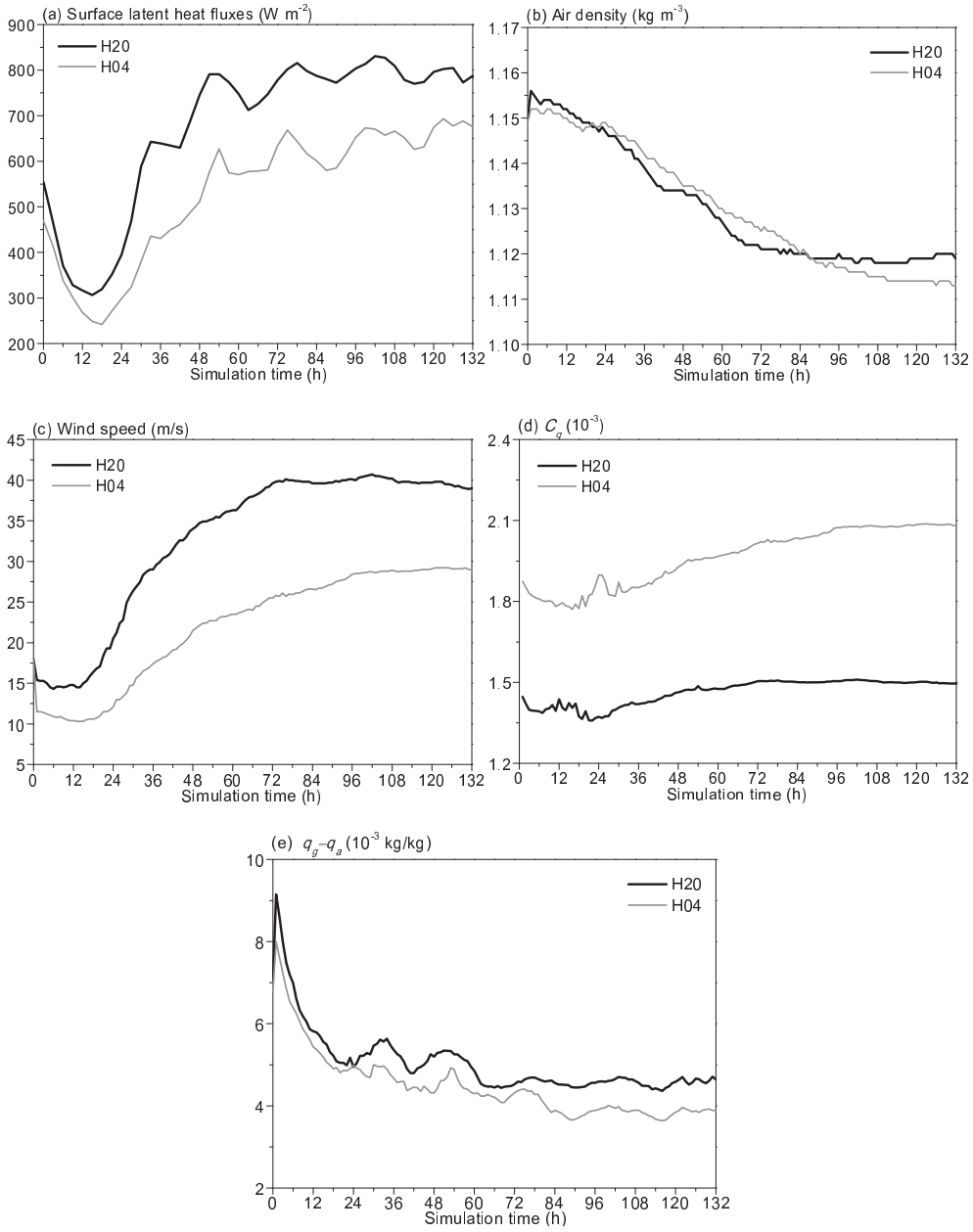


**Fig. 6.** Time series of (a) the surface latent heat fluxes (W $m^{-2}$), (b) the air density (kg $m^{-3}$) in the SL, (c) the wind speed (m $s^{-1}$) at the LML, (d) surface moisture exchange coefficient ($10^{-3}$) and (e) the mixing ratio difference ($10^{-3}$ kg $kg^{-1}$) between the surface and the LML. The averaging is done within a radius of 150 km from each experiment's respective storm center.

(Fig. 6c). For the case with a higher LML, the mixing ratio difference was correspondingly larger. These results suggest that the wind speed at the LML and the mixing ratio difference between the surface and the LML are the two major factors regulating the changes in surface latent heat fluxes caused by varying the LML height.

In an attempt to further investigate the cause of the sensitivity of these variables, the vertical profiles of azimuthally-averaged air density, wind speed and vapor mixing ratio at the RMW were examined, and the results are shown in Fig. 7. The time was taken at 126 h because both runs had analogous RMW values at that time (Fig. 3). The profiles of air density in H20 and H04 were close to each other, both varying little with height in the boundary layer. The difference of their values at the LML was fairly small, 0.011 kg $m^{-3}$, only accounting for 1% of the density in H04, which further confirmed the negligible contribution of air density to the changes in surface heat fluxes. The simulated wind fields (Figs. 7b) showed typical logarithmic features that changed rapidly with height in the near-surface layer (Powell et al., 2003) and then approached more constant values, suggesting a good capability of the modified YSU scheme in producing a

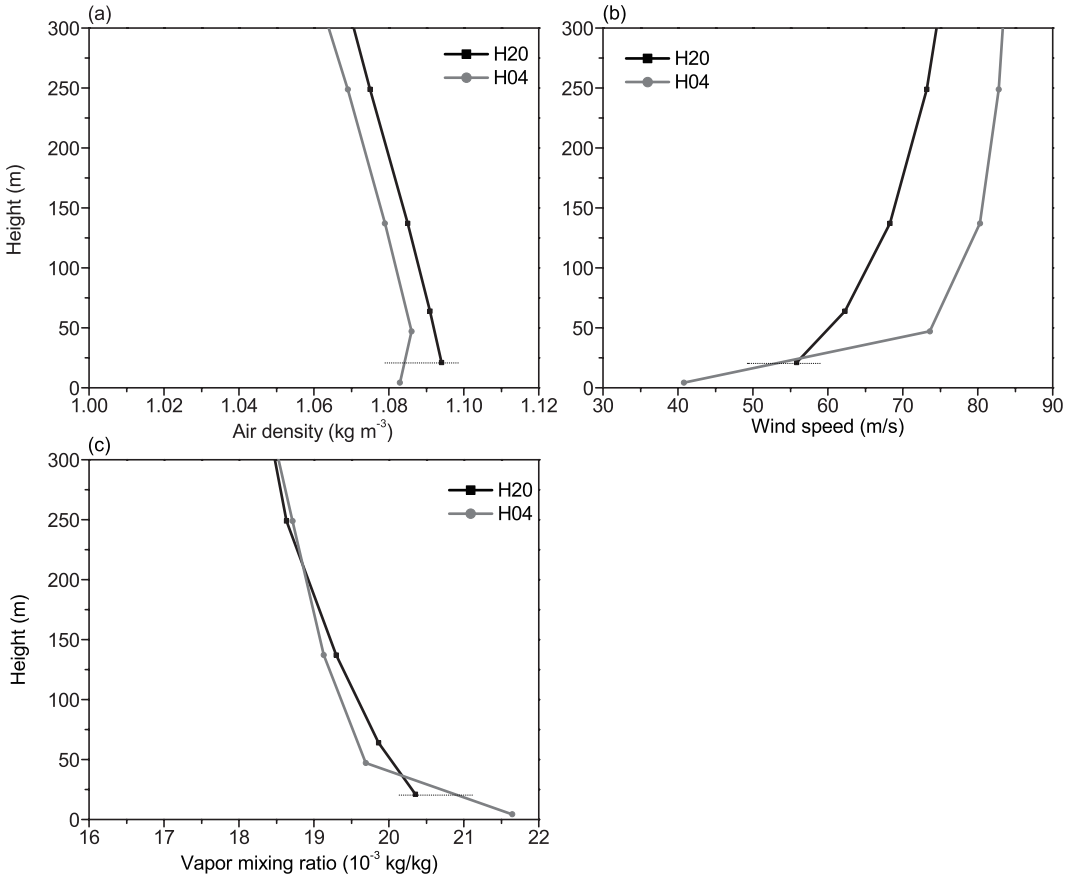


**Fig. 7.** The vertical profiles of azimuthally-averaged (a) air density (kg m$^{-3}$), (b) wind speed (m s$^{-1}$), and (c) vapor mixing ratio ($10^{-3}$ kg kg$^{-1}$) at the radius of maximum surface winds at 126 h. The solid squares and circles indicate the heights of the actual model levels for H20 and H04, respectively.

logarithmic surface layer. The wind speed at the LML in H20 was larger than in H04, which was shown to be caused not only by their differences in profiles but also by their different heights. The water vapor mixing ratio also exhibited a similar logarithmic characteristic near the surface (Hobbs et al., 2002) and then decreased slowly with height for the two runs (Fig. 7c). H20 yielded lower humidity than H04 at the LML, and thus $(q_g - q_a)$ should have been amplified [Eq. (6)]. At 126 h, $q_g$ was approximately $25.1 \times 10^{-3}$ kg kg$^{-1}$ for the two runs (not shown); their simulated profiles appeared similar, indicating the difference of $(q_g - q_a)$ was caused mainly by the difference of the LML height.

These results imply that the surface heat fluxes were considerably sensitive to the LML height. The wind speed was the leading ingredient manipulating the changes in surface latent heat fluxes, wherein the differences of the wind speeds at the LML were caused not only by their simulated profile differences but also by their different heights. Another important contributor was the humidity, which depended mainly on the height it was taken from. Nonetheless, the mixing ratio difference between the surface and the LML became smaller with time. This may have been because the TCs basically remained stationary during the simulation so that $q_a$ got close to the saturated value gradually due to the presence of downdrafts. For moving TCs, the contribution of mixing ratio difference is expected to be larger and the results may be somewhat different. The surface moisture coefficient would decrease as the LML rises, and thus offset the contributions of wind speed and humidity. Because of the logarithmic characteristics of wind speed and other meteorological variables in the SL, the LML-induced changes in surface heat fluxes are expected to be more significant as the LML height decreases, but less significant as the LML ascends.

### 4.3. *Physical mechanisms*

To further understand how the variation of LML affects TC evolution, the thermodynamic and dynamic features of simulated TCs were investigated. Figure 8 compares the Hovmöller diagram of equivalent potential temperature at 0.1 km in altitude for H20 and H04. Since the increase of equivalent potential temperature following the air parcel relies largely on the upward surface latent and sensible heat fluxes (warming through sensible heat fluxes, moistening through latent heat fluxes, and isothermal expansion) from the ocean (Rotunno and Emanuel, 1987; Liu et al., 1999), the equivalent potential temperature increased radially inward to a maximum in the eye region as a result of flow converging into the TC center. Despite its weaker intensity in the later stage,

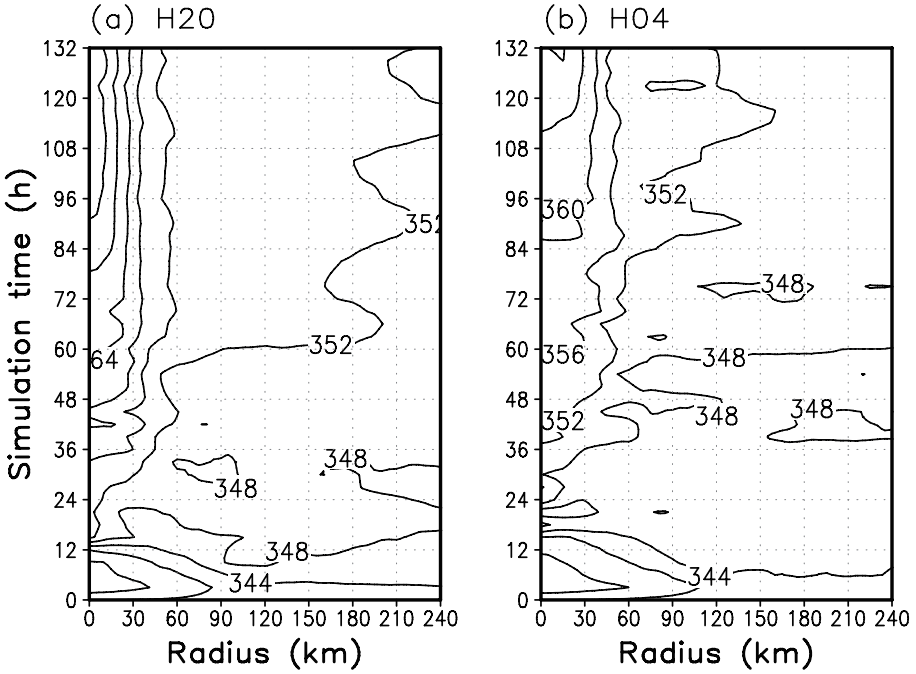


**Fig. 8.** Hovmöller diagram of azimuthally-averaged equivalent potential temperature (K) for (a) H20 and (b) H04 at 0.1 km in altitude.

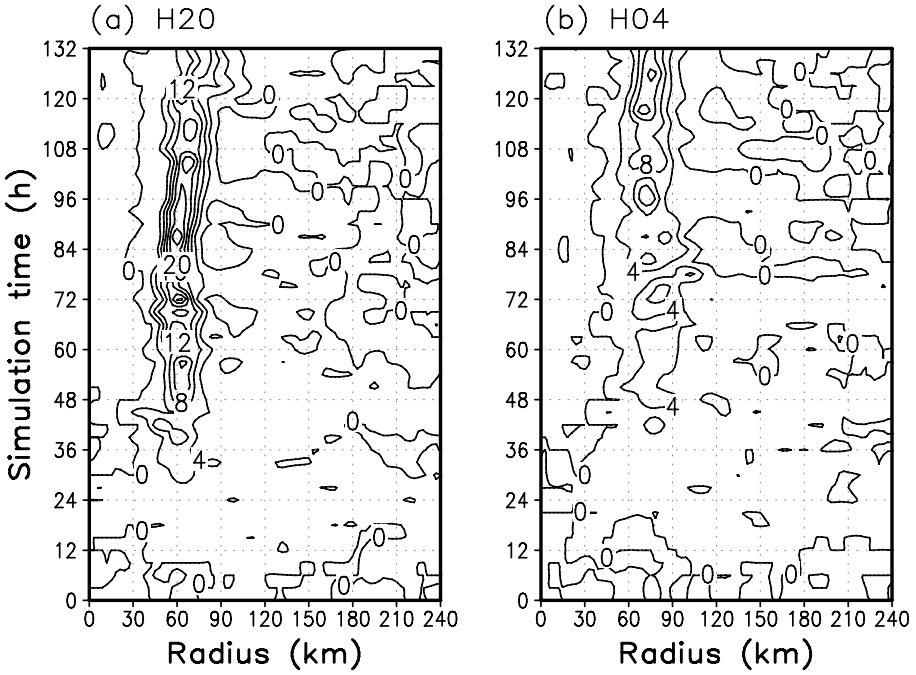


**Fig. 9.** Hovmöller diagram of azimuthally-averaged diabatic heating ($10^{-3}$ K $s^{-1}$) output directly from WRF for (a) H20 and (b) H04 at model level $\eta$=0.507 (about 5.3 km in altitude).

the storm in H20 possessed higher equivalent potential temperature throughout the simulation, arising from its enhanced surface heat fluxes (Fig. 6a). Therefore, the air flow entering the inner-core region tended to be more energetic and thus helped yield more energy for eyewall convection.

Figure 9 displays the time evolution of the azimuthally-averaged diabatic heating rate at about 5.3 km in altitude for H20 and H04, which was outputted directly from the WRF model. Due to the tilt of the eyewall (Figs. 4b and e), the diabatic heating rate was located outside the RMW (Fig. 3). Evidently, the diabatic heating was substantially stronger in H20 due to the presence of enhanced surface heat fluxes, and was therefore conducive to inducing stronger primary and secondary circulations (Shapiro and Willoughby, 1982; Bui et

al., 2009; Fudeyasu and Wang, 2011). The diabatic heating in H20 primarily concentrated in the eyewall region, while outside the eyewall it was fairly weak—a reflection of the inhibited inner rainband activity by strong filamentation outside the eyewall (Wang, 2008a, 2008b). In contrast, the diabatic heating in H04 seemed to be relatively active outside the eyewall, though its value was small, which led to a larger storm in H04 than in H20 (Xu and Wang, 2010a). The stronger diabatic heating in H20 also led to more strengthened inward contraction of the RMW (Fig. 3) and therefore the decrease in the eye size (Shapiro and Willoughby, 1982; Wang, 2008b; Xu and Wang, 2010b).

The above analysis demonstrates that a higher LML induced significant changes in TC thermodynamic features, including enhanced surface moisture fluxes and low-level equivalent potential temperature, and more intense diabatic heating in the eyewall region. However, the storm did not consequently possess unanimously stronger intensity, but instead became weaker in terms of MSLP after about 114 h. Such an inconsistency between the storm intensity and surface enthalpy fluxes implies that another mechanism manipulating the storm evolution could have been influenced by changing the LML height, namely the surface friction effects (Shapiro and Willoughby, 1982), which play dual roles in TC intensification. Firstly, the frictional stress disrupts the gradient wind balance in the boundary layer and induces radial convergence of the air flow, which brings larger absolute angular momentum inward and spins up the inner-core primary circulation (Smith et al., 2009). Secondly, the friction is a sink of kinetic energy of TCs and acts to restrict the storm from intensifying (Zhang et al., 2006; Wu et al., 2009; Wang and Xu, 2010; Liu et al., 2011; Yang et al., 2011).

Figure 10 shows the time series of $C_{d10}$ for H20 and H04 to denote the surface friction effects. H20 showed much larger values than H04, suggesting the surface friction was stronger in H20. Even in the later stage when H04 produced a stronger storm in terms of MSLP (Fig. 1a), its friction effects were still weaker than H20. Figure 11 shows the Hovmöller diagrams of low-level radial winds. Because of more intense diabatic heating in the eyewall and surface dissipation, the boundary radial flow in H20 tended to be stronger than in H04 (Shapiro and Willoughby, 1982; Bui et al., 2009; Fudeyasu and Wang, 2011). Yang et al. (2011) verified that the tangential flow is weakened but the low-level radial inflow is reinforced due to increased surface friction during TC landfall. Elevating the LML seemed to produce similar effects; that is, as the surface friction increased progressively with the storm's strengthening, the primary circulation appeared to be more weakened in the later stage in H20 (Figs. 3 and 12), while its boundary radial flow remained stronger (Figs. 11 and 12). The outflow that appeared in the low-level eyewall (Fig. 12) helped maintain the supergradient wind in the boundary layer, which is a ubiquitous characteristic of a TC (e.g., Kepert and Wang, 2001; Kepert, 2006; Nolan et al., 2009b). H20 produced stronger outflow relative to H04 in the later stage (Fig. 12), even though its tangential winds were weaker.

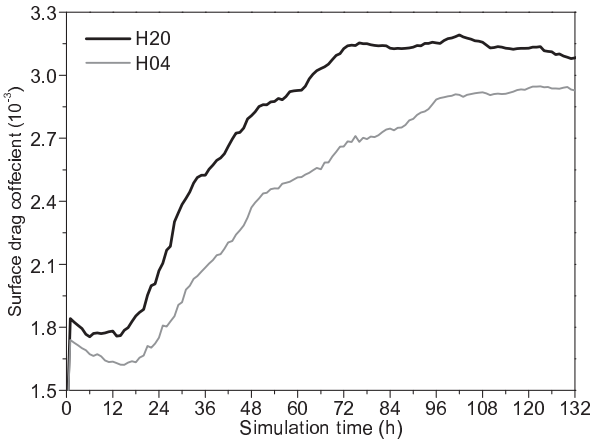


**Fig. 10.** (a) Time series of 10-m surface momentum exchange coefficient ($10^{-3}$). The averaging is done within a radius of 150 km from each experiment's respective storm center.

## 5. Discussion

One typical feature of the SL is the logarithmic profiles of meteorological variables. In this case, changes of these variables become more dramatic when their height gets closer to the surface. Therefore, the sensitivity of TC intensity to the selection of LMLs seems to be greater for lower LMLs, whereas weaker for higher LMLs (Fig. 1). The convective boundary layer characteristics of TCs render the commonly used LMLs well within the real SL. The results of H20 and H04 exemplified the remarkable influences of the LML on TC intensity and internal structures, even when the LML was placed properly in the real SL. According to the sensitivity experiments in this study, the LML height is expected to not be shallower than 12 m, so that the performance of the SL scheme will not be quite sensitive to the LML height. Meanwhile, a thin modeled SL is expected to fully represent the SL characteristics and help improve the vertical resolutions. For instance, Zhang and Wang (2003) suggested a thin SL (20 m) to be used after their sensitivity simulations. Based on the above analysis, an LML with its height ranging from 12–20 m seems to be appropriate for TC modeling.

One interesting finding was that, although the surface latent heat fluxes were enhanced by elevating the LML, the ultimate TC intensity in terms of MSLP did not deepen as a result. This is different from the results of Kimball and Dougherty (2006), who found an over-intensified storm caused by an LML that was "too high". A possible reason for the difference between their conclusion and this study lies in the experimental designs. For instance, one of their experiments adopted an LML placed at 348 m, which should correspond to a PBL height of at least 3480 m, far above the typical height scales of the TC boundary layer (Kepert and Wang, 2001; Smith et al., 2010; Zhang et al., 2011). Besides, such an LML is close to the region where maximum tangential winds occur, and thus the contribution of surface heat fluxes could be greatly exaggerated.

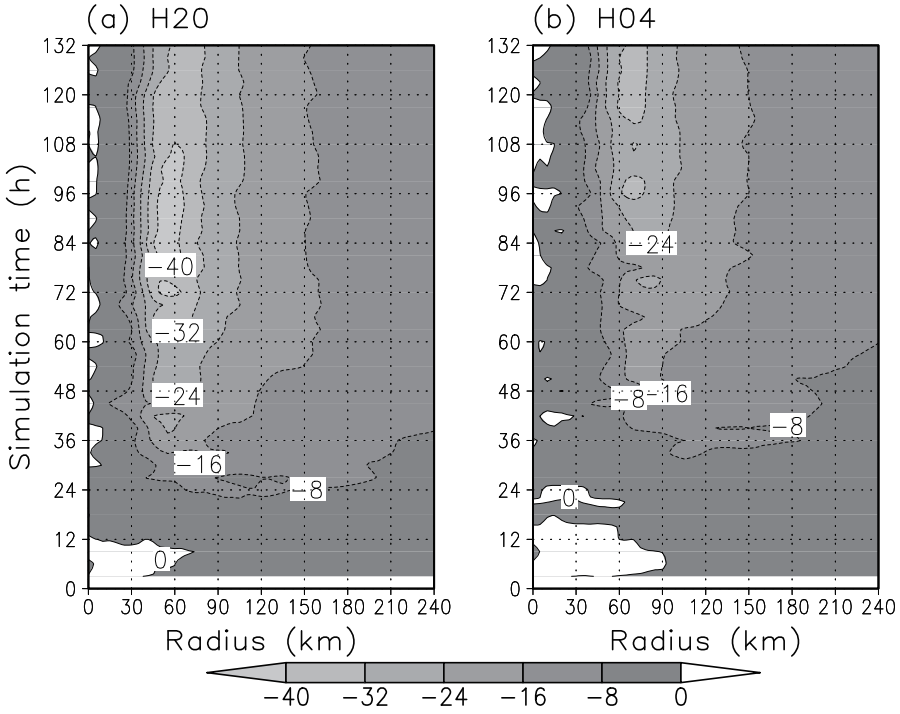


**Fig. 11.** Hovmöller diagram of the azimuthally-averaged radial winds (m $s^{-1}$) for (a) H20 and (b) H04 at 0.1 km in altitude.

Nolan et al. (2007) diagnosed the TC intensification issue using balanced vortices without considering the frictional boundary layer and showed that the TC intensification rate is proportional to the intensity itself. However, in this study H20 produced a much greater intensification rate but similar deepest intensity compared to H04 (Fig. 1a), indicating that besides convectional heating, the surface frictional force played a crucial role in modulating the TC intensification process. Nevertheless, the conventional Charnock relationship may overemphasize the surface friction associated with the surface roughness under high wind regimes. We conducted an additional series of experiments by assigning the roughness length to be homogenously 0.0002 m, a typical value over smooth water, so that the surface friction effect was greatly reduced and the friction difference between H20 and H04 could be alleviated considerably. In that case, both runs simulated storms that were more strengthened than before, and the storm in H20 was evidently stronger than in H04 throughout the simulation (not shown), further identifying the weakening effects of surface friction on storm development. Although the time evolutions of MSLP between H20 and H12 were similar in the early stage, some discrepancy appeared in the last 30 h. This was because the weakening of H12 was delayed compared with H20 due to their difference in the simulated SL characteristics.

Surface heat fluxes and surface friction are the most important exchange components for TC–ocean coupling and TC–wave coupling models, respectively (e.g., Zhu et al., 2004; Zhang et al., 2006; Liu et al., 2011). Considering the notable influences of the LML height on both surface heat fluxes and surface friction effects, a proper placement of the LML should be specified in air–sea–wave coupling models to avoid over- or under-evaluating ocean feedback. The outer rainbands of the simulated storms were not active in this study. For storms with active outer spiral rainbands, elevating the LML may lead to a different storm size evolution (Wang, 2009; Xu and Wang, 2010a), which needs further investigation.

As indicated in Fig. 1, during the later stage the intensity relationship between H20 and H04 in terms of VMAX10 exhibited opposite behavior from that in terms of MSLP, a reflection of the changed wind–pressure relationships by varying the LML. During this time period the trend of tangential winds was consistent with that of MSLP (Fig 3), while the trend of radial winds was consistent with that of VMAX10 (Fig. 11). A possible reason for the shallower MSLP but stronger VMAX10 in H20 than in H04 could be that, although H20 did not produce evidently stronger tangential winds in the later stage, its radial winds were still stronger due to the enhanced surface friction, therefore producing larger total surface winds in H20 than in H04. This suggests that radial wind is a crucial factor for the wind–pressure relationships, as recently suggested by Kieu et al. (2010).

## 6. Conclusion

The effects of the LML height on simulated TCs were examined through comparing a series of idealized experiments with different LMLs. The results identified notable influences of the LML on TC evolution.

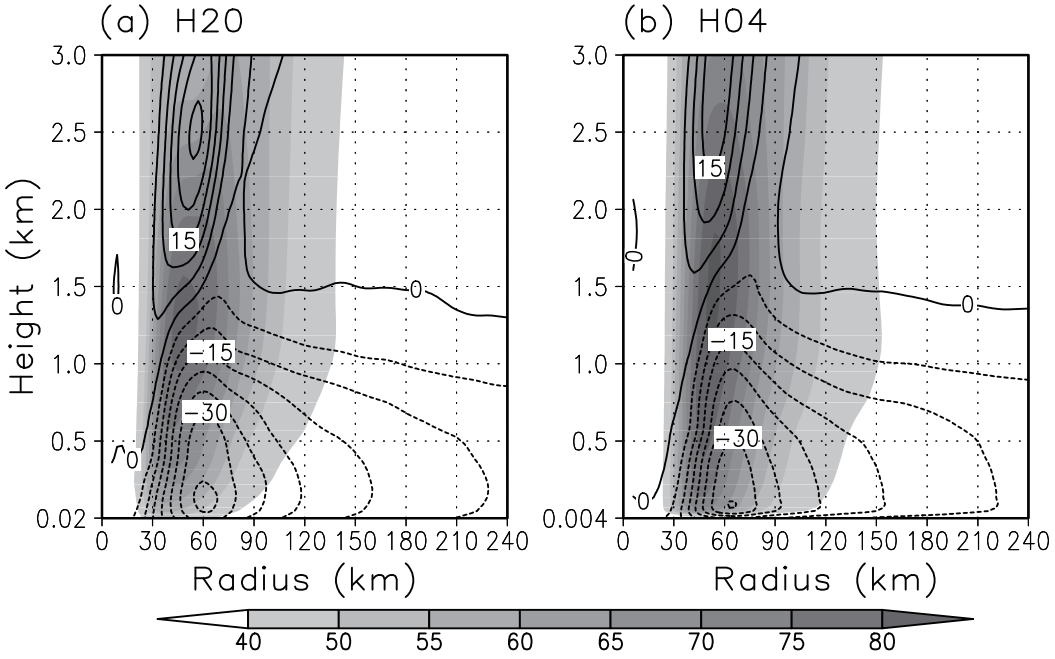


**Fig. 12.** Height–radius cross sections of the azimuthally-averaged radial winds (contour; m $s^{-1}$) and tangential winds (shaded; m $s^{-1}$) for (a) H20 and (b) H04 at 126 h.

When the LML was above 12 m, the sensitivity of the simulated TC to the selection of LML seemed to be weak. However, when the LML was placed below 12 m, the storm intensification rate decreased evidently with the LML descending that during the intensification process an MSLP difference of 30 hPa could be attained by changing the LML height. Nevertheless, the eventual intensity changes caused by different LML heights were relatively small. Inconsistent with the trend of MSLP, VMAX10 was generally larger for a higher LML, and thus the wind–pressure relationships were consequently changed. The tangential winds were more strengthened in the early stage but weakened slightly in the later stage for the experiment with a higher LML, similar to the behavior of MSLP. VMAX10 seemed to be not as revealing as MSLP and the structural metrics in terms of azimuthally-averaged tangential winds, as argued in recent studies. Elevating the LML also led to a more contracted storm circulation.

The LML produces effects on storms through directly changing near-surface variables. In the present study, surface latent heat fluxes were greatly enhanced throughout the simulation by elevating the LML, although this did not result in an eventually stronger storm in terms of MSLP. By evaluating each term comprising the computation of surface latent heat fluxes, the wind speed at the LML was identified to dominate the changes of surface latent heat fluxes, followed by the mixing ratio difference between the surface and the LML. The contribution of changes in air density caused by varying the LML was negligible. The surface moisture exchange coefficient played an offsetting role since it decreased with height. A diagnosis of vertical profiles of these variables suggested that changes in wind speeds were dependent on not only their profile differences, but also the different heights they were taken from. For the mixing ratio difference, the simulated profile discrepancies were small, and thus the different heights that the water vapor mixing ratio was taken from could have played a dominant role.

The enhanced surface heat fluxes by elevating the LML led to greater low-level equivalent potential temperature and more intense eyewall convection. As a consequence, the diabatic heating was increased, which contributed to more rapid storm intensification, as well as stronger secondary circulation. Since the diabatic heating mainly concentrated in the eyewall region, it contributed mainly to the eyewall contraction but little to the expansion of outer circulation. Stronger surface friction was also produced by a higher LML, which resulted in weakened tangential flow but strengthened radial inflow in the later stage.

Despite the fact that the roles of LML in TC modeling have received little attention before, the present study has confirmed that the LML has significant impacts on TC evolution when it is below a certain height. For studies on TC modeling issues including TC intensification, wind–pressure relationships, TC–ocean interaction and TC–wave interaction, cautions is recommended when deciding upon the placement of the LML. It should be noted that stationary TCs were adopted in this study, in which case the mixing ratio of water vapor at the LML was able to become gradually saturated with storm intensification. However, if the TC is allowed to move, the results may be somewhat different. Additionally, the underlying model surface in this study was set to a uniform ocean. Over the land surface, where the surface fluxes are computed by a land-surface model, the roles of the LML still need further investigation.

***Acknowledgements.*** We are grateful to Prof. Yuqing WANG, Prof. Da-Lin ZHANG and the two anonymous reviewers for their constructive and detailed comments, which helped a lot in improving the manuscript. This work was supported by the National Public Benefit (Meteorology) Research Foundation of China (Grant No. GYHY201106004) and the National Natural Science Foundation of China (Grant Nos. 41005029, 41105065 and 41230421).

## REFERENCES

Aligo, E. A., W. A. Gallus Jr., and M. Segal, 2009: On the impact of WRF model vertical grid resolution on Midwest summer rainfall forecasts. *Wea. Forecasting*, **24**, 575–594.

Anthes, R. A., and S. W. Chang, 1978: Response of the hurricane boundary layer to changes of sea surface temperature in a numerical model. *J. Atmos. Sci.*, **35**, 1240–1255.

Arya, S. P., 1988: *Introduction to Micrometeorology*. Academic Press, 307 pp.

Bao, J.-W., S. G. Gopalakrishnan, S. A. Michelson, F. D. Marks, and M. T. Montgomery, 2012: Impact of physics representations in the HWRFX on simulated hurricane structure and pressure–wind relationships. *Mon. Wea. Rev.*, **140**, 3278–3299.

Bui, H. H., R. K. Smith, M. T. Montgomery, and J. Y. Peng, 2009: Balanced and unbalanced aspects of tropical cyclone intensification. *Quart. J. Roy. Meteor. Soc.*, **135**, 1715–1731.

Chen, H., D.-L. Zhang, J. Carton, and R. Atlas, 2011: On the rapid intensification of Hurricane Wilma (2005). Part I: Model prediction and structural changes. *Wea. Forecasting*, **26**, 885–901.

Dudhia, J., 1989: Numerical study of convection observed during the Winter Monsoon Experiment using a mesoscale two-dimensional model. *J. Atmos. Sci.*, **46**, 3077–3107.

Dyer, A. J., and B. B. Hicks, 1970: Flux-gradient relationships in the constant flux layer. *Quart. J. Roy. Meteor. Soc.*, **96**, 715–721.

Emanuel, K. A., 1986: An air-sea interaction theory for tropical cyclones. Part I: Steady-state maintenance. *J. Atmos. Sci.*, **43**, 585–604.

Fudeyasu, H., and Y. Q. Wang, 2011: Balanced contribution to the intensification of a tropical cyclone simulated in TCM4: Outer-core spinup process. *J. Atmos. Sci.*, **68**, 430–449.

Gentry, M. S., and G. M. Lackmann, 2010: Sensitivity of simulated tropical cyclone structure and intensity to horizontal resolution. *Mon. Wea. Rev.*, **138**, 688–704.

Hobbs, S., D. Dyer, D. Courault, A. Olioso, J.-P. Lagouarde, Y. Kerr, J. Mcaneney, and J. Bonnefond, 2002: Surface layer profiles of air temperature and humidity measured from unmanned aircraft. *Agron. Sustain. Dev.*, **22**, 635–640.

Holton, J. R., 2004: *An Introduction to Dynamic Meteorology*. Academic Press, 529 pp.

Hong, S. Y., Y. Noh, and J. Dudhia, 2006: A new vertical diffusion package with an explicit treatment of entrainment processes. *Mon. Wea. Rev.*, **134**, 2318–2341.

Jiménez, P. A., J. Dudhia, J. F. González-Rouco, J. Navarro, J. P. Montávez, and E. García-Bustamante, 2012: A revised scheme for the WRF surface layer formulation. *J. Atmos. Sci.*, **140**, 898–918.

Jordan, C. L., 1958: Mean soundings for the West Indies area. *J. Meteor.*, **15**, 91–97.

Kain, J. S., 2004: The Kain-Fritsch convective parameterization: An update. *J. Appl. Meteor.*, **43**, 170–181.

Kepert, J. D., 2006: Observed boundary layer wind structure and balance in the hurricane core. Part II: Hurricane Mitch. *J. Atmos. Sci.*, **63**, 2194–2211.

Kepert, J. D., and Y. Q. Wang, 2001: The dynamics of boundary layer jets within the tropical cyclone core. Part II: Nonlinear enhancement. *J. Atmos. Sci.*, **58**, 2485–2501.

Kieu, C. Q., H. Chen, and D.-L. Zhang, 2010: An examination of the pressure–wind relationship for intense tropical cyclones. *Wea. Forecasting*, **25**, 895–907.

Kimball, S. K., and F. C. Dougherty, 2006: The sensitivity of idealized hurricane structure and development to the distribution of vertical levels in MM5. *Mon. Wea. Rev.*, **134**, 1987–2008.

Knaff, J. A., and R. M. Zehr, 2007: Reexamination of tropical cyclone wind–pressure relationships. *Wea. Forecasting*, **22**, 71–88.

Lin, Y. L., R. D. Farley, and H. D. Orville, 1983: Bulk parameterization of the snow field in a cloud model. *J. Appl. Meteor. Climatol.*, **22**, 1065–1092.

Liu, B., H. Q. Liu, L. Xie, C. L. Guan, and D. L. Zhao, 2011: A coupled atmosphere–wave–ocean modeling system: Simulation of the intensity of an idealized tropical cyclone. *Mon. Wea. Rev.*, **139**, 132–152.

Liu, Y. B., D.-L. Zhang, and M. K. Yau, 1999: A multiscale numerical study of Hurricane Andrew (1992). Part II: Kinematics and inner-core structures. *Mon. Wea. Rev.*, **127**, 2597–2616.

Ma, Z. H., J. F. Fei, L. Liu, X. G. Huang, and X. P. Cheng, 2013: Effects of the cold core eddy on tropical cyclone intensity and structure under idealized air-sea interaction conditions. *Mon. Wea. Rev.*, **141**, 1285–1303.

Mlawer, E. J., S. J. Taubman, P. D. Brown, M. J. Iacono, and S. A. Clough, 1997: Radiative transfer for inhomogeneous atmospheres: RRTM, a validated correlated-k model for the longwave. *J. Geophys. Res.*, **102**, 16 663–16 682.

Monin, A. S., and A. M. Obukhov, 1954: Basic laws of turbulent mixing in the atmosphere near the ground. *Tr. Inst. Teor. Geofiz. Akad. Nauk SSSR*, **24**, 163–187.

Nolan, D. S., Y. Moon, and D. P. Stern, 2007: Tropical cyclone intensification from asymmetric convection: Energetics and efficiency. *J. Atmos. Sci.*, **64**, 3377–3405.

Nolan, D. S., J. A. Zhang, and D. P. Stern, 2009a: Evaluation of planetary boundary layer parameterizations in tropical cyclones by comparison of in situ observations and high-resolution simulations of Hurricane Isabel (2003). Part I: Initialization, maximum winds, and the outer-core boundary layer. *Mon. Wea. Rev.*, **137**, 3651–3674.

Nolan, D. S., D. P. Stern, and J. A. Zhang, 2009b: Evaluation of planetary boundary layer parameterizations in tropical cyclones by comparison of in situ observations and high-resolution simulations of Hurricane Isabel (2003). Part II: Inner-core boundary layer and eyewall structure. *Mon. Wea. Rev.*, **137**, 3675–3698.

Paulson, C. A., 1970: The mathematical representation of wind speed and temperature profiles in the unstable atmospheric surface layer. *J. Appl. Meteor.*, **9**, 857–861.

Powell, M. D., 1990: Boundary layer structure and dynamics in outer hurricane rainbands. Part II: Downdraft modification and mixed layer recovery. *Mon. Wea. Rev.*, **118**, 918–938.

Powell, M. D., P. J. Vickery, and T. A. Reinhold, 2003: Reduced drag coefficient for high wind speeds in tropical cyclones. *Nature*, **422**, 279–283.

Rotunno, R., and K. A. Emanuel, 1987: An air-sea interaction the-

ory for tropical cyclones. Part II: Evolutionary study using a non-hydrostatic axisymmetric numerical model. *J. Atmos. Sci.*, **44**, 542–561.

Shapiro, L. J., and H. E. Willoughby, 1982: The response of balanced hurricanes to local sources of heat and momentum. *J. Atmos. Sci.*, **39**, 378–394.

Shin, H. H., S. Y. Hong, and J. Dudhia, 2012: Impacts of the lowest model level height on the performance of planetary boundary layer parameterizations. *Mon. Wea. Rev.*, **140**, 664–682.

Skamarock, W. C., J. B. Klemp, J. Dudhia, D. O. Gill, D. M. Barker, W. Wang, and J. G. Powers, 2008: A description of the advanced research WRF version 3. NCAR Tech. Note NCAR/TN-475+STR, 113 pp.

Smith, R. K., M. T. Montgomery, and N. Van Sang, 2010: Hurricane boundary-layer theory. *Quart. J. Roy. Meteor. Soc.*, **136**, 1665–1670.

Smith, R. K., and M. T. Montgomery, and V. S. Nguyen, 2009: Tropical cyclone spin-up revisited. *Quart. J. Roy. Meteor. Soc.*, **135**, 1321–1335.

Stern, D. P., and D. S. Nolan, 2011: On the vertical decay rate of the maximum tangential winds in tropical cyclones. *J. Atmos. Sci.*, **68**, 2073–2094.

Stern, D. P., and D. S. Nolan, 2012: On the height of the warm core in tropical cyclones. *J. Atmos. Sci.*, **69**, 1657–1680.

Stull, R. B., 1988: *An Introduction to Boundary Layer Meteorology*. Springer, 666 pp.

Wang, Y. Q., 2008a: Rapid filamentation zone in a numerically simulated tropical cyclone. *J. Atmos. Sci.*, **65**, 1158–1181.

Wang, Y. Q., 2008b: Structure and formation of an annular hurricane simulated in a fully compressible, nonhydrostatic model—TCM4. *J. Atmos. Sci.*, **65**, 1505–1527.

Wang, Y. Q., 2009: How do outer spiral rainbands affect tropical cyclone structure and intensity? *J. Atmos. Sci.*, **66**, 1250–1273.

Wang, Y. Q., and J. Xu, 2010: Energy production, frictional dissipation, and maximum intensity of a numerically simulated tropical cyclone. *J. Atmos. Sci.*, **67**, 97–116.

Webb, E. K., 1970: Profile relationships: The log-linear range, and extension to strong stability. *Quart. J. Roy. Meteor. Soc.*, **96**, 67–90.

Wei, H., M. Segal, W. J. Gutowski Jr., Z. Pan, R. W. Arritt, and W. A. Gallus Jr., 2001: Sensitivity of simulated regional surface thermal fluxes during warm advection snowmelt to selection of the lowest model level height. *J. Hydrometeor.*, **2**, 395–405.

Wu, C.-C., H.-J. Cheng, Y. Q. Wang, and K.-H. Chou, 2009: A numerical investigation of the eyewall evolution in a landfalling typhoon. *Mon. Wea. Rev.*, **137**, 21–40.

Xu, J., and Y. Q. Wang, 2010a: Sensitivity of tropical cyclone inner-core size and intensity to the radial distribution of surface entropy flux. *J. Atmos. Sci.*, **67**, 1831–1852.

Xu, J., and Y. Q. Wang, 2010b: Sensitivity of the simulated tropical cyclone inner-core size to the initial vortex size. *Mon. Wea. Rev.*, **138**, 4135–4157.

Yang, M.-J., D.-L. Zhang, X.-D. Tang, and Y. Zhang, 2011: A modeling study of Typhoon Nari (2001) at landfall: 2. Structural changes and terrain-induced asymmetries. *J. Geophys. Res.*, **116**, D09112, doi: 10.1029/2010JD015445.

Yau, M. K., Y. B. Liu, D.-L. Zhang, and Y. S. Chen, 2004: A multiscale numerical study of Hurricane Andrew (1992). Part VI: Small-scale inner-core structures and wind streaks. *Mon. Wea. Rev.*, **132**, 1410–1433.

Zängl, G., A. Gohm, and F. Obleitner, 2008: The impact of the PBL scheme and the vertical distribution of model layers on simulations of Alpine foehn. *Meteor. Atmos. Phys.*, **99**, 105–128.

Zhang, D.-L., and R. A. Anthes, 1982: A high-resolution model of the planetary boundary layer—Sensitivity tests and comparisons with SESAME-79 data. *J. Appl. Meteor.*, **21**, 1594–1609.

Zhang, D.-L., and X. X. Wang, 2003: Dependence of hurricane intensity and structures on vertical resolution and time-step size. *Adv. Atmos. Sci.*, **20**, 711–725.

Zhang, D.-L., and H. Chen, 2012: Importance of the upper-level warm core in the rapid intensification of a tropical cyclone. *Geophys. Res. Lett.*, **39**, L02806, doi: 10.1029/2011GL050578.

Zhang, J. A., R. F. Rogers, D. S. Nolan, and F. D. Marks Jr., 2011: On the characteristic height scales of the hurricane boundary layer. *Mon. Wea. Rev.*, **139**, 2523–2535.

Zhang, W. Q., W. Perrie, and W. B. Li, 2006: Impacts of waves and sea spray on midlatitude storm structure and intensity. *Mon. Wea. Rev.*, **134**, 418–442.

Zhu, H. Y., U. Wolfgang, and R. K. Smith, 2004: Ocean effects on tropical cyclone intensification and inner-core asymmetries. *J. Atmos. Sci.*, **61**, 1245–1258.